JOURNAL OF PROPULSION AND POWER
Vol. 16, No. 6, November–December 2000

Computation of Gas–Liquid Droplet Cascade Flows Using Multigrid Adaptive Unstructured Grid

Ki-Cheol Park*
Samsung Aerospace Industries, Ltd., Changwon City, Kyungnam 641-717, Republic of Korea
and
Keun-Shik Chang†
Korea Advanced Institute of Science and Technology, Yusong-gu, Taejon 305-701, Republic of Korea

Two-dimensional transonic cascade flows of gas–liquid droplet mixture are calculated using the solution-adaptive unstructured grid for the steady gas-only phase and the iterative particle-source-in-cell method for the gas–particle coupling. Roe's flux difference splitting method is used to solve the Euler equations, whereas the liquid droplets are traced by the Lagrangian method using the rebound/breakup impact model. To verify accuracy of the computer code, the Jet Propulsion Laboratory nozzle is first calculated for the gas–solid particle mixture. The transonic flow in the NACA 65410 cascade passage is then solved to estimate the effect of liquid droplets on the aerodynamic performance.

Nomenclature

a	=	speed of sound
C_D	=	drag coefficient
$C_{p,g}$	=	specific heat of the gas at constant pressure
$C_{p,p}$	=	specific heat of the particle
D_p	=	particle diameter
$h_{\min}$	=	minimum height of a triangular element
L_∞	=	characteristic length
M_p	=	particle Mach number, $\sqrt{[(u-u_p)^2+(v-v_p)^2]}/a$
m_p	=	particle mass
N_p	=	particle number density per unit volume
N_{pa}	=	particle number density per unit volume after impact
N_{pb}	=	particle number density per unit volume before impact
$\dot{N}_{p,k}$	=	number flow rate for kth particle
Nu	=	Nusselt number
Pr	=	Prandtl number
p	=	pressure
p_b	=	outlet (background) pressure
q	=	velocity of the particle
R	=	gas constant
Re_p	=	particle Reynolds number, $\rho\lvert\boldsymbol{u}-\boldsymbol{u}_p\rvert D_p/\mu$
T	=	temperature
$\boldsymbol{u}$	=	velocity vector (u, v) of the gas
$\boldsymbol{u}_p$	=	velocity vector (u_p, v_p) of the particle
We	=	Weber number, $\rho\lvert\boldsymbol{u}-\boldsymbol{u}_p\rvert^2 D_p/\sigma$
We_d	=	droplet Weber number, $\rho_p\lvert q_n\rvert^2 D_p/\sigma$
γ	=	specific heat ratio
ΔS	=	entropy change, $S-S_\infty$
Δt_p	=	local particle time step for particle motion
ε	=	internal energy
μ	=	dynamic viscosity coefficient of the gas
ρ	=	density
σ	=	surface tension of the water
φ	=	particle mass loading, $N_p \cdot m_p/\rho$

Subscripts

a	=	flow property after the droplet impact
b	=	flow property before the droplet impact
n	=	in normal direction
p	=	particle property
t	=	in tangential direction
∞	=	freestream property

Superscript

n	=	time level

Introduction

IN the natural environment, we find water in all phases as vapor, liquid, or ice, which includes snow and hail. An airbreathing gas turbine engine as an aircraft power plant sometimes ingests this environmental water. Liquid water entering the engine could be either precipitation, inlet condensation, droplet suspension, or artificial liquid spray during the ground test. In particular, safety of aircraft in a heavy rainstorm during cruise or descent has become a critical issue among aerodynamicists. Some researchers investigated the performance degradation of the aircraft lifting surface due to the heavy rain.[1] A more serious problem is ingestion of an excessive amount of precipitation that may cause power loss or even flameout of the engine to endanger the aircraft.[2]

Despite the significant volume of research about the turbomachinery cascade flow, the number of publications on the particulated two-phase flow is limited. Tabakoff et al.[3] calculated one-dimensional isentropic flow in the turbine cascade to evaluate degradation of turbine performance by the particulated flow. He found that the change of pressure distribution on the turbine blade due to interaction with the solid particles resulted in decreased performance. Tsuchiya and Murthy[4] using the stage-stacking method calculated the change of performance in the multistage axial compressor due to rain drop ingestion. They found that rain drop ingestion caused a decrease in the total pressure ratio, adiabatic efficiency, and mass flow rate. However, their study was concerned with general compressor performance rather than elaborating the detailed flow structure. Murthy[2] has recently performed an experimental study on two-phase flow in single- and multistage compressors using a range of droplet size and mass fractions. The results showed that the single-stage compressor suffered from the heavy aerodynamic loss in the blade tip region, which caused serious performance degradation in the case of a multistage compressor. Reference 5 offers a list and summary of published works on the subject until 1995. However, most of these works are again concerned with prediction of the overall engine performance rather than an analysis of the detailed turbomachinery flowfields.

Received 2 September 1999; revision received 4 February 2000; accepted for publication 7 February 2000.

*Senior Researcher, Research Team 2, Engine Engineering Center, 28, Sungju-Dong.
†Professor, Department of Aerospace Engineering 373-1 Kusong-dong.

In this paper a numerical method is presented to calculate the transonic cascade exposed to water-droplet suspension. An adaptive unstructured multigrid code using the Euler equations and the Lagrangian particle-tracking scheme is developed. The iterative particle-source-in-cell (PSIC) method is used to implement the effect of liquid droplet motion in the gas phase through the source terms that evolve with numerical iteration. The two-phase flow properties in the cascade passage are elaborated in the Results and Discussion section.

Numerical Formulation

The Euler equations are written in conservative form,

$$\frac{\partial \boldsymbol{U}}{\partial t} + \frac{\partial \boldsymbol{F}_i}{\partial x_i} + j\boldsymbol{H} = \boldsymbol{S}, \qquad (i = 1, 2) \tag{1}$$

with

$$\boldsymbol{U} = \begin{pmatrix} \rho \\ \rho u \\ \rho v \\ \rho \varepsilon \end{pmatrix}, \qquad \boldsymbol{F}_1 = \begin{pmatrix} \rho u \\ \rho u^2 + p \\ \rho uv \\ u(\rho\varepsilon + p) \end{pmatrix}, \qquad \boldsymbol{F}_2 = \begin{pmatrix} \rho v \\ \rho vu \\ \rho v^2 + p \\ v(\rho\varepsilon + p) \end{pmatrix} \tag{2}$$

$$\boldsymbol{H} = \frac{1}{y}\begin{pmatrix} \rho v \\ \rho vu \\ \rho v^2 \\ v(\rho\varepsilon + p) \end{pmatrix}, \qquad \boldsymbol{S} = \begin{pmatrix} S_m \\ S_u \\ S_v \\ S_\varepsilon \end{pmatrix} \tag{3}$$

$$p = (\gamma - 1)\rho\left[\varepsilon - \tfrac{1}{2}(u^2 + v^2)\right] \tag{4}$$

where $j = 0$ for the two-dimensional flow and $j = 1$ for the axisymmetric flow. $\boldsymbol{H}$ is the axisymmetric source vector, and $\boldsymbol{S}$ is the particle source vector. The equations are nondimensionalized using a characteristic length L_∞ and freestream properties ρ_∞, a_∞, T_∞, and μ_∞.

Roe's flux difference splitting method is used to calculate the numerical fluxes. The primary and dual meshes shown in Fig. 1 are the basic finite volumes used to compute the flux terms and the particle sources at the same time. To achieve second-order accuracy in space, the least-square method by Anderson and Bonhaus[6] and the flux limiter by Venkatakrishnan[7] are used. Based on the unstructured triangular mesh initially generated by the advancing-front technique, the multigrid and adaptive grids are obtained by the element refinement/unrefinement algorithm.[8] In the time direction, explicit four-stage Runge–Kutta time stepping is applied.

Coupling Between Phases

We assume that there is heat transfer but no phase change or mass transfer between the two phases. Dilute particle suspension is assumed[9] so that collisions among the droplets can be neglected. The Lagrangian particle motion is described by the ordinary differential equations

$$\frac{du_p}{dt_p} = D_n(u - u_p), \qquad \frac{dv_p}{dt_p} = D_n(v - v_p) \tag{5}$$

with

$$D_n = \tfrac{3}{4}(\rho/\rho_p)(C_D/D_p)\Delta V \cdot L_\infty \tag{6}$$

$$\Delta V = \sqrt{(u - u_p)^2 + (v - v_p)^2} \tag{7}$$

The expressions for the particle drag coefficient C_D are summarized for convenience.[5,10]

For the solid particles:

$$C_D = \left(C_{D_0} - 2\right)\exp\left[-3.07\sqrt{\gamma}(M_p/Re_p)g(Re_p)\right] + [h(M_p)/\sqrt{\gamma}M_p]\exp[-(Re_p/2M_p)] + 2 \tag{8}$$

with

$$C_{D_0} = \begin{cases} 24/Re_p, & 0 < Re_p < 0.34 \\ 0.48 + 28Re_p^{-0.85}, & 0.34 < Re_p < 10^5 \end{cases}$$

$$h(M_p) = [5.6/(M_p + 1)] + 1.7\sqrt{T_p/T}$$

$$g(Re_p) = \frac{1 + Re_p(12.278 + 0.584Re_p)}{1 + 11.278Re_p}, \qquad Re_p < 10^3 \tag{9}$$

For the liquid droplets:

$$C_D = \begin{cases} 24/Re_p, & Re_p < 1 \quad \text{(Stokes law)} \\ (21.64/Re_p) + 2.36, & 1 < Re_p < 10 \\ \left(21.942/Re_p^{0.718}\right) + 0.324, & Re_p > 10 \end{cases} \tag{10}$$

We allow droplet deformation and disintegration due to the shear force using the technique given in Ref. 5. From Eq. (5), we advance the particle velocity by

$$u_p^{n+1} = u^n - \left(u^n - u_p^n\right)e^{(-D_n\Delta t_p)}$$

$$u_p^{n+1} = u^n - \left(u^n - u_p^n\right)e^{(-D_n\Delta t_p)} \tag{11}$$

The new particle position is then

$$x_p^{n+1} = x_p^n + (\Delta t_p/2)\left(u_p^{n+1} + u_p^n\right)$$

$$y_p^{n+1} = y_p^n + (\Delta t_p/2)\left(v_p^{n+1} + v_p^n\right) \tag{12}$$

Assuming that there is no phase change, the particle temperature is obtained by

$$\frac{dT_p}{dt_p} = \Gamma_n(T - T_p) \tag{13}$$

$$T_p^{n+1} = T^n - \left(T^n - T_p^n\right)e^{(-\Gamma_n\Delta t_p)} \tag{14}$$

with

$$\Gamma_n = 6(Nu/Pr)(\mu/\rho_p)(1/\rho_\infty)(L_\infty/a_\infty)\left(1/D_p^2\right)(C_{p,g}/C_{p,p}) \tag{15}$$

Nussel Number Nu is given as follows.[4,11]

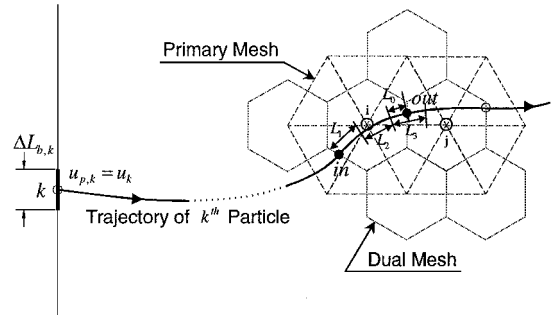

Fig. 1 Particle streakline and summation of particle number flow rate in a control volume.

Solid particles:

$$Nu = \frac{Nu_0}{1 + 3.42[M_p/(Re_p Pr)]Nu_0} \tag{16}$$

with

$$Nu_0 = 2 + 0.459 Re_p^{0.55} Pr^{0.33} \tag{17}$$

Liquid droplets:

$$Nu = 2 + 0.6 Re_p^{0.5} Pr^{0.33} \tag{18}$$

The particle source vector $\boldsymbol{S}$ is generated by the momentum and heat transfer between the gas and particle phases and is

$$\boldsymbol{S} = \begin{pmatrix} 0 \\ F_{PX} \\ F_{PY} \\ Q_P + u_p F_{PX} + v_p F_{PY} \end{pmatrix} \tag{19}$$

where

$$F_{PX} = (\pi/8) D_p^2 \rho C_D (u_p - u) \Delta V \left(1 \Big/ L_\infty^2\right)$$

$$F_{PY} = (\pi/8) D_p^2 \rho C_D (v_p - v) \Delta V \left(1 \Big/ L_\infty^2\right)$$

$$Q_P = \pi/(\gamma - 1)(D_p/L_\infty)(Nu/Pr)(\mu/\rho_\infty a_\infty L_\infty)(T_p - T) \tag{20}$$

The gas–droplet interaction is treated by the PSIC procedure.[12] The steady gas-only phase is first computed without the particle source terms in the Euler equations by the four-stage Runge–Kutta time-stepping method using the local time steps and multigrid procedure. Based on this Euler solution, the particle streak lines are traced in the flow domain. Initially the particle number flow rate is specified at the sampling points uniformly distributed on the inlet boundary, as shown in Fig. 1 for one such a point. A local particle time step Δt_p is used that is defined by

$$\Delta t_p = \min(\Delta t, 0.3 h_{\min}/|\boldsymbol{u}_p|) \tag{21}$$

In each finite volume, the particle source terms are calculated using the particles accumulated.

Given the initial distribution of source terms, coupling between the gas and the particle phase is made as follows. The Euler equations with the source terms [Eq. (1)] are solved to the steady state by the so-called inner cycle. This solution provides gas flow data that are used in solving the Lagrangian equations of particle motion initially. The particle streaklines are then generated in the flow domain. With the particle source terms calculated by Eq. (22) (to be given), Eq. (1) is solved again. This process is called an outer cycle. We continue this iterative procedure until the two-phase coupling is fully converged within a small tolerance.

In the outer cycle, a particle can stay in a control volume for a few number of particle time steps before it crosses the cell boundary. For example, L_1, L_2, and L_3 in Fig. 1 represent, respectively, the distance traveled by a particle during the consecutive particle time steps in an outer cycle, for example, $\Delta t_{p,1}$, $\Delta t_{p,2}$, and $\Delta t_{p,3}$. In the time step $\Delta t_{p,3}$, the particle changes its host control volume from i to j. The fraction of time step $\Delta t_{p,3}$ consumed by the particle in the particular control volume i, for example, $\Delta t_{p,0}$, is calculated by assuming that the particle velocity is locally constant in the small control volume for a small particle time step. The source vector in the control volume i is then obtained by

$$\boldsymbol{S}_i = \sum_{k=1}^{K} \sum_{j=0}^{J} \boldsymbol{S}_{i,j}^k \cdot \dot{N}_{p,k} \cdot \Delta t_{p,j} \tag{22}$$

with

$$\dot{N}_{p,k} = N_p u_{p,k} \Delta L_{b,k} L_\infty^3 \tag{23}$$

where K is the total number of droplets passing through the control volume i at a given time and J is the total number of particle time steps consumed by a droplet before it leaves the control volume i.

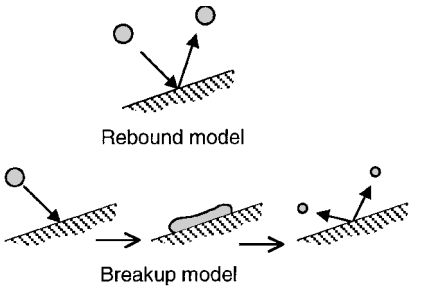

Fig. 2 Droplet impact model.

Droplet Breakup and Impact Model

Raindrops are assumed of spherical shape in size varying from 20 μm to several millimeters. The droplets can undergo rapid shape change to irregular disks and possibly to shear breakup in the inlet passage of the engine. Unfortunately, it is difficult to determine the actual size and density distributions of the droplets because they depend on the engine operating conditions as well. The effect of droplet deformation can be approximated by multiplying 1.0 to the droplet coefficient C_D in Eq. (10), for $We/\sqrt{(Re)_p} = 0$, and by multiplying 1.7, for $We/\sqrt{(Re_p)} = 0.79$, with linear interpolation in between. When $We/\sqrt{(Re_p)} > 0.79$ and $\mathrm{d}[We/\sqrt{(Re_p)}]/\mathrm{d}t > 30$, the original droplets break into smaller droplets, the size distribution of which can be determined using the approach introduced in Ref. 5.

As shown in Fig. 2, when the droplet impacts the blade, it may rebound or break up depending on the droplet Weber number. This phenomenon is the subject of another large research area.[13] Here we employed the rather simple droplet rebound/breakup models proposed by Park and Watkins,[14] which are given next.

For the rebound model where $We_{d,b} < 80$,

$$q_{n,a} = -(We_{d,a}/We_{d,b})^{0.5} q_{n,b} \tag{24}$$

$$q_{t,a} = q_{t,b} \tag{25}$$

$$D_{p,a} = D_{p,b} \tag{26}$$

For each impacting droplet, $We_{d,b}$ is calculated, and $We_{d,a}$ is obtained by curve fitting the Wachters and Westering data (see Ref. 14).

For the breakup model where $We_{d,b} > 80$, droplets resulted from the breakup have additional velocity called the film propagating velocity q_f, which is given by

$$q_f = 0.835(3.096 - 2\chi) q_{n,b} \tag{27}$$

with $\chi = 1.28$. It is assumed that the original droplet breaks into two representative droplets. The droplet tangential velocity after breakup is given by

$$q_{t,a} = q_{t,b} \pm R_{xx} q_f \tag{28}$$

where R_{xx} is a random number in (0, 1).

The normal velocity component, diameter, and number density of the droplets after breakup are obtained, respectively, by

$$q_{n,a} = -\left(\frac{\sigma We_{d,a}}{\rho_p D_{p,a}}\right)^{0.5} \tag{29}$$

$$D_{p,a} = D_{p,b}/m_{\text{break}}^{\frac{1}{3}} \tag{30}$$

$$N_{pa,1} = N_{pa,2} = 0.5\, N_{pb} m_{\text{break}} \tag{31}$$

with

$$m_{\text{break}} = 0.187\, We_b - 14 \tag{32}$$

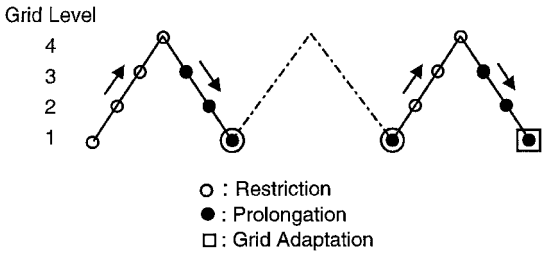

Fig. 3 Multigrid cycles for the gas-only phase with a grid adaptation made in a few iterations.

Multigrid Convergence Acceleration

The multigrid convergence acceleration technique is commonly used on structured grids, but there still are some problems when applied to the unstructured grids. In particular, it is of much concern to generate successive fine and coarse grids in a consistent manner with less complexity. The adaptive unstructured multigrid technique in this paper is based on the successive mesh refinement/unrefinement technique comparable to that of Connel and Holmes[15] and Parthasarathy and Kallinderis.[16] It is used to obtain the gas-phase solution before it is allowed to couple with the droplet phase iteratively. Brandt's full-approximation scheme and simple sawtooth multigrid cycles (shown in Fig. 3) are used.

The multigrid is constructed as follows. The coarsest grid, called grid of level 4, is first generated by the advancing-front technique. Finer grids of lower levels are next constructed by successive grid refinement. At the finest grid of level 1, when the gas-phase solution converges after some multigrid cycles, the grid is adapted to the flow by grid refinement/unrefinement again. The coarser grids are generated from this by grid unrefinement. In Figs. 4a–4d, the multigrids used in the gas-only phase calculation are sampled. The grid in Fig. 4d shows the finest grid of level 1 obtained by grid refinement and three consecutive flow adaptions afterwards. Convergence rate of this flow-adaptive multigrid method is compared with that of the single grid in Fig. 5, which shows a remarkable convergence acceleration.

Results and Discussion

Two-Phase Flow in a Jet Propulsion Laboratory Nozzle

Cuffel et al.[17] published in 1969 the test data for the gas-only phase in the Jet Propulsion Laboratory (JPL) nozzle. This nozzle, originally designed for experimental purpose, has since served as a benchmark problem for the numerical study of nozzle flows.[18] Chang[19] and Ishii and Umeda[20] used the Eulerian–Eulerian approach to calculate the gas–solid particle mixture in the JPL nozzle. Hwang and Chang[21] showed that similar results could be obtained on the structured grid by the Eulerian–Lagrangian approach.

To verify the present computer code, we first reproduce the gas–solid particle two-phase JPL nozzle flow studied by Ishii and Umeda.[20] The geometry of the JPL nozzle is given in Fig. 6 and the computational grid in Fig. 7. The material properties of the gas and the particle used in this study can be found in Ref. 20. Figure 8 shows that the present result for the gas-only phase is in good agreement with the test data. For the two-phase flow, we chose two particle sizes, $D_p = 2\ \mu$m and $D_p = 6\ \mu$m, following Ishii and Umeda for comparison purposes. The Mach number distribution on the nozzle axis and wall shows good agreement in Fig. 9. The effect of particle on the nozzle properties can be viewed in Fig. 10. Flow deceleration by the particles, especially by the smaller sized particles can be clearly seen. As a convergence criterion, we took the rms value of the density residual less than 10^{-6} for the inner cycle and 2×10^{-5} for the outer cycle. The numerical results were virtually unchanged even though the convergence criteria were further lowered by an order of magnitude. Convergence was slower with the smaller particle sizes. The overall computation time decreased when the iteration number in the inner cycle was near optimal. For instance, for the case of the particle diameter 6 μm, when 100 time steps were taken in the inner cycle to solve the Euler equations before its solution was allowed to interact with the particles, it required 30 iterations in the outer cycle or total 2948 time steps for convergence of the two-phase solution. In contrast, when 1,000 iterations were used in the inner cycle, only 14 iterations were necessary in the outer cycles or total 11,489 overall time steps. Figures 11a and 11b show the convergence history in the inner cycle and outer cycle, respectively. If a small iteration number was taken in the inner cycle, then a large iteration number would result in the outer cycle, and vice versa. In

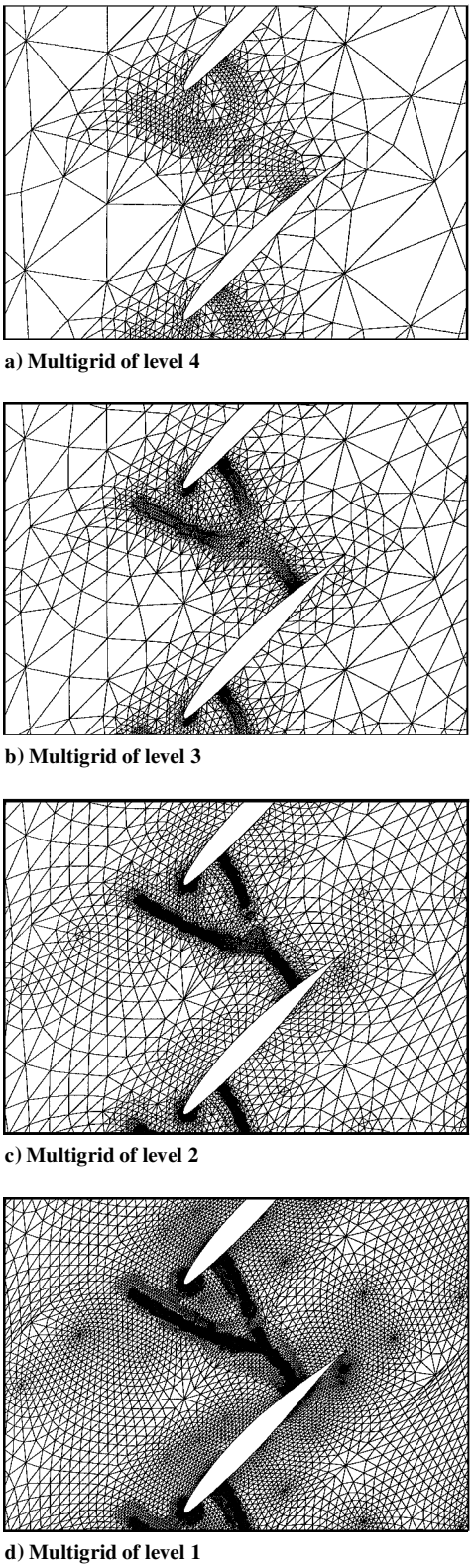

a) Multigrid of level 4

b) Multigrid of level 3

c) Multigrid of level 2

d) Multigrid of level 1

Fig. 4 Unstructured multigrid used for the gas-only phase.

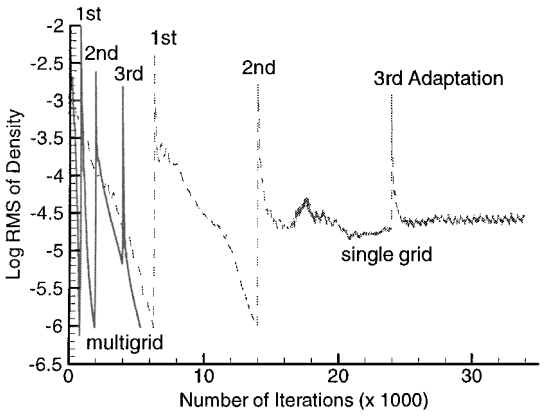

Fig. 5 Comparison of convergence rate between single and multigrid solution.

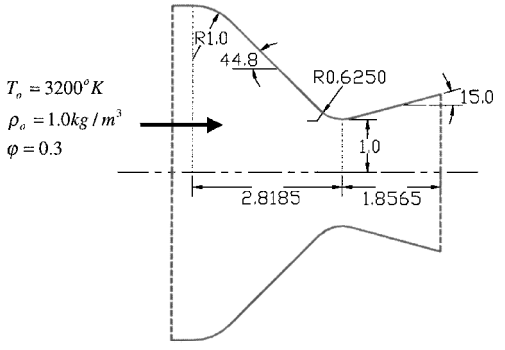

Fig. 6 Schematic of the JPL nozzle (coordinate is scaled by throat radius).

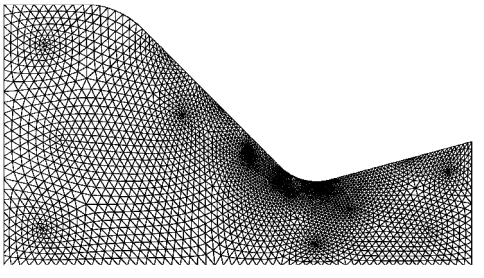

Fig. 7 Computational grid for the JPL nozzle.

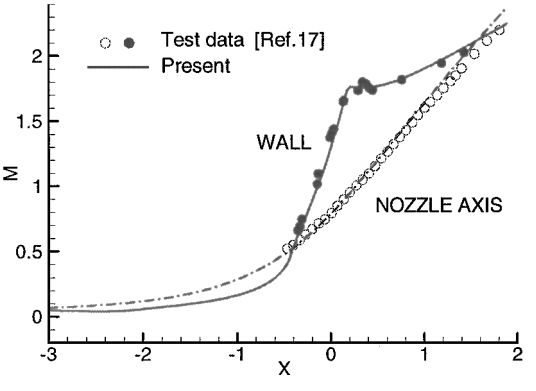

Fig. 8 Mach number distribution on the nozzle wall and central axis (gas-only phase).

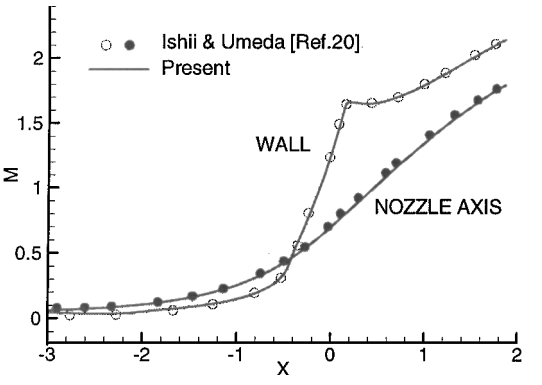

Mach number distribution for $D_p = 6\ \theta$ m

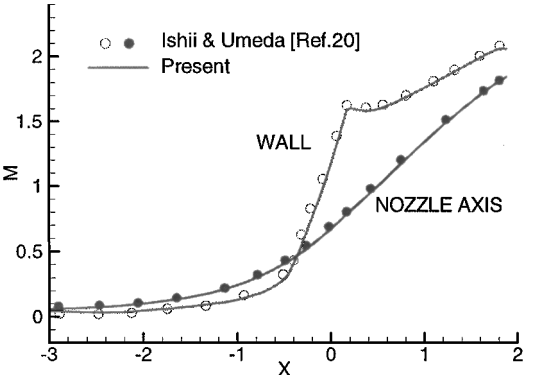

Mach number distribution for $D_p = 2\ \theta$ m

Fig. 9 Two-phase JPL nozzle flows (φ = 0.3).

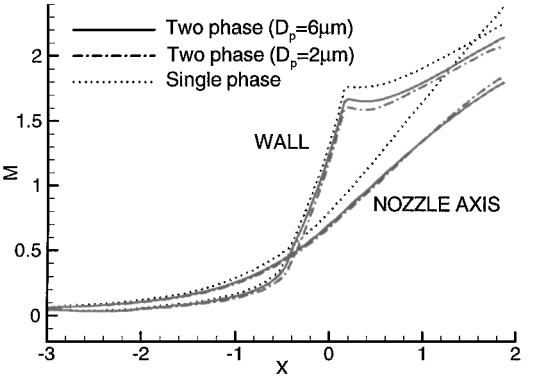

Fig. 10 Comparison of Mach number distributions between single- and two-phase flows (φ = 0.3).

the Table in Fig. 11b, which includes two more cases of 10 and 5000 iterations in the inner cycle, one can observe that case B, 100 iterations in the inner cycle, offers the fastest convergence.

Transonic Flows in NACA 65410 Cascade

The present cascade geometry was chosen from an earlier study.[22] The flow conditions were taken as follows, which simulate a set of typical experimental conditions. The blade has physical chord length 300 mm, stagger angle 45 deg, and inlet flow angle 53 deg. It has resultant inlet Mach number 0.981 for the gas-only phase, inlet total pressure 1 atm, and inlet total temperature 290 K. For computational accuracy, the steady nonreflecting boundary conditions by Giles[23] are employed. We imposed the zero normal flux and normal velocity condition on the impermeable boundary and the periodic flow condition on the fictitious boundary between the blades. Figure 12 shows the computational domain and the nondimensional coordinates used in the discussion to follow.

In this paper we consider liquid droplets of size 20 μm, following the practice of Tsuchiya and Murthy.[4] We assume 5% water mass

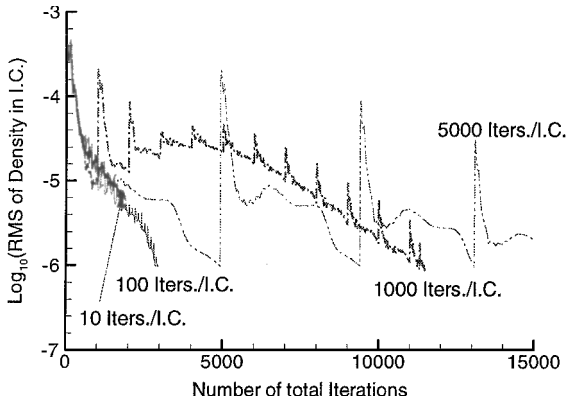

a) Inner cycle

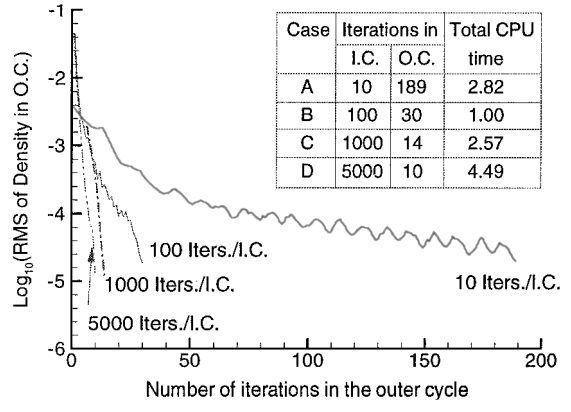

Case	Iterations in		Total CPU
	I.C.	O.C.	time
A	10	189	2.82
B	100	30	1.00
C	1000	14	2.57
D	5000	10	4.49

b) Outer cycle

Fig. 11 Two-phase flow, $\varphi = 0.3, D_p = 6\ \theta$ m, convergence history.

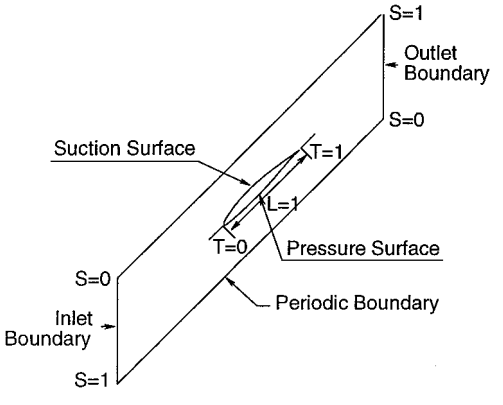

Fig. 12 Dimensionless coordinates of the boundary on computational domain.

concentration in accordance with U.S. MIL-SPEC. In the present problem, there appeared no droplet disintegration by the shock wave, as was verified by the formula given in Ref. 5. Contours of the steady-state Mach number and pressure are compared in Figs. 13a and 13b for the single- and two-phase flows, respectively. The liquid droplets cause the passage shock to move downstream, whereas the bow shock in front of the cascade retreats as the shock is weakened. The thermodynamic losses caused by the momentum transfer and heat transfer between the two phases cause the entropy increase in the cascade. In Fig. 14a, the average inlet Mach number of the two-phase flow, 0.955, is observed to be lower than that of the single-phase flow, 0.981, when the outlet static pressure is fixed identically in the two flows. On the outlet boundary, the exit Mach number is increased relatively more on the suction side than on the pressure side in comparison with the single phase. On the outlet boundary,

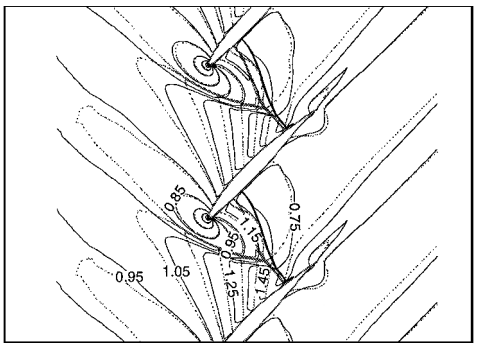

a) Mach number contours ($\Delta M = 0.1$)

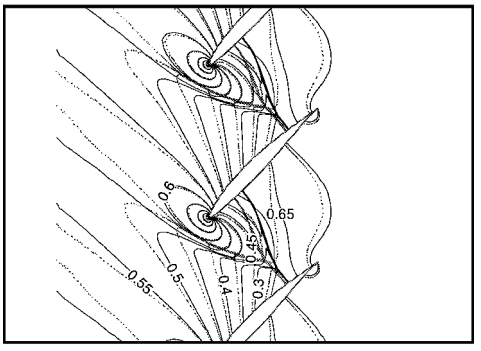

b) Pressure contours ($\Delta p = 0.05$)

Fig. 13 Single- and two-phase flows in the cascade ($\varphi = 0.05, D_p = 20\ \theta$ m, $p_b = 1.0$): ——, two phase, and - - - -, single phase.

the total pressure of the two-phase flow is higher than that of the single phase as observed in Fig. 14b.

In the single phase, the total temperature remains constant throughout the cascade passage because the present cascade is stationary without any shaft work input. In the particulated flow, however, the total temperature of the gas should vary in the flowfield due to the momentum transfer and heat transfer between the two phases. The temperature and velocity of the gas phase are higher than that of the single phase on both sides of the shock. As a consequence, the two-phase flow has higher total temperature on the outlet boundary, as one can see from Fig. 14c. For this reason, as in Fig. 14d, the entropy increment on the outlet boundary is higher in the two-phase flow even though the outlet total pressure is increased. It is well known that water ingestion moves the engine operating line upward,[5] which corresponds to reducing the inlet mass flow rate or the inlet Mach number. Present results are in accordance with this phenomenon.

In Figs. 15a and 15b, pressure and Mach number distributions on the surface of the two-phase cascade are given, respectively. The shock waves are moved toward the trailing edge despite the reduced inlet Mach number, as compared to the single-phase flow. The intensity of the shock on the suction side is weakened, whereas the shock on the pressure side is moved aft quite a bit.

In Figs. 16a and 16b, the Mach number contours for the two- and single-phase flows are displayed, respectively. About the same average inlet Mach number conditions are used a posteriori: 0.955 for the two-phase flow and 0.961 for the gas-only phase. Note that, in the gas-only phase, the shock on the pressure surface disappeared and the shock on the suction surface was moved upstream. The shock impinging on the pressure surface was so weak that it disappeared when the inlet Mach number was further reduced. The bow shock wave in the front is moved upstream as its strength is weakened in the two-phase flow.

Droplets change the aerodynamic properties of the blade considerably. With the same inlet Mach number or mass flow rate in the single- and two-phase flows, the static pressure and Mach number distributions on the blade surface are significantly altered, as one

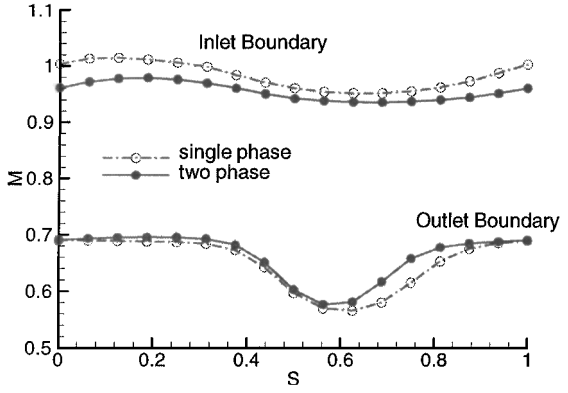

a) Mach number

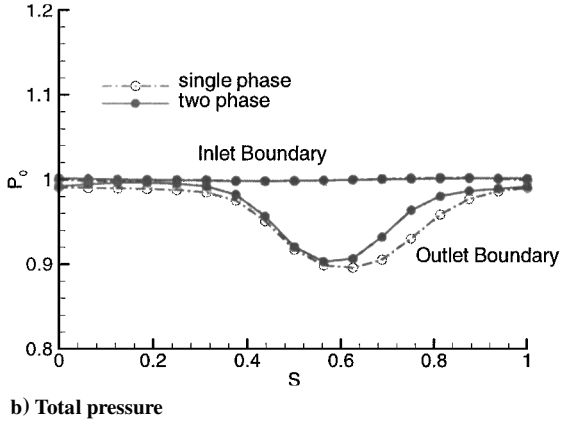

b) Total pressure

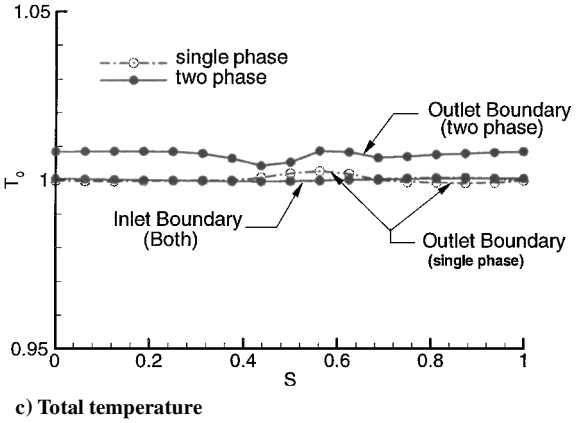

c) Total temperature

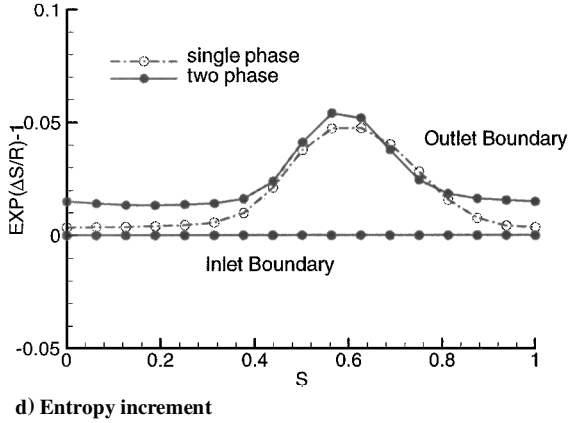

d) Entropy increment

Fig. 14 Droplet effect on the inlet and outlet boundaries.

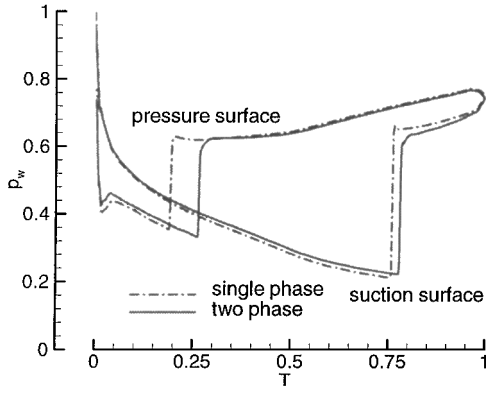

a) Surface pressure

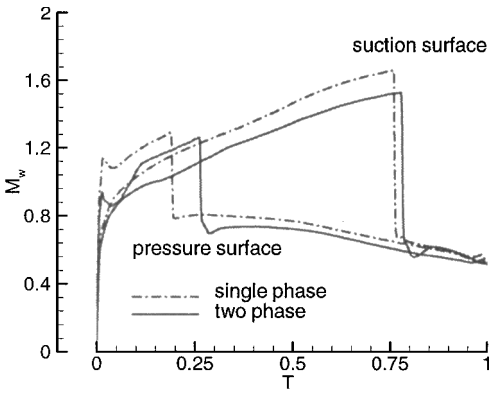

b) Surface Mach number

Fig. 15 Droplet effect on the blade properties (with p_b = 1.0).

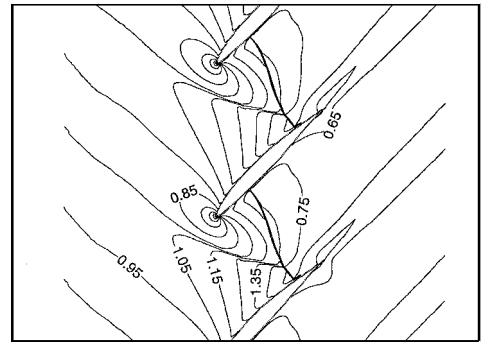

a) Two-phase flow: $M_{in} = 0.955$, adaptation level 3, $\varphi = 0.05$, $D_p = 20\,\theta$ m, P_b = 1.0

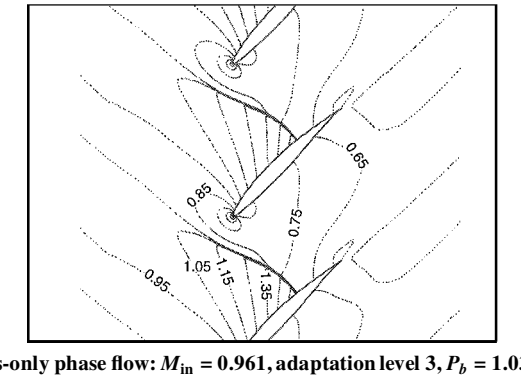

b) Gas-only phase flow: $M_{in} = 0.961$, adaptation level 3, P_b = 1.03

Fig. 16 Droplet effect on the Mach number contours (ΔM = 0.1).

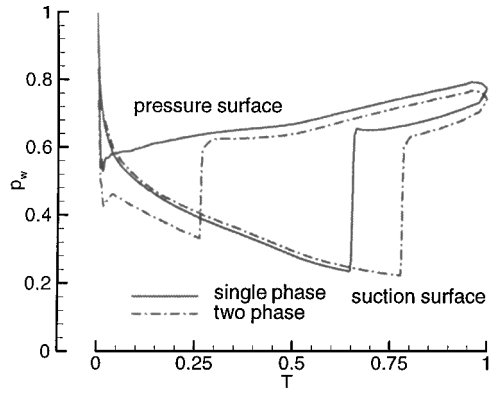

a) Surface pressure: $M_{in} \approx 0.96$

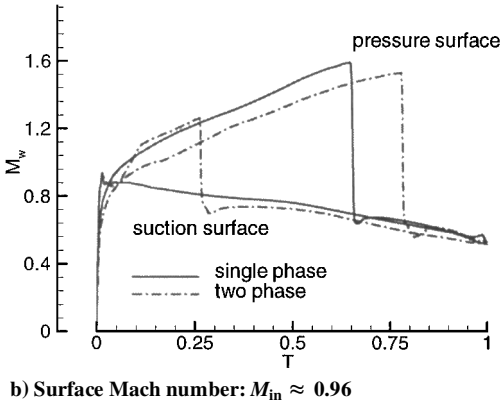

b) Surface Mach number: $M_{in} \approx 0.96$

Fig. 17 Droplet effect on the blade properties (with fixed inlet Mach number).

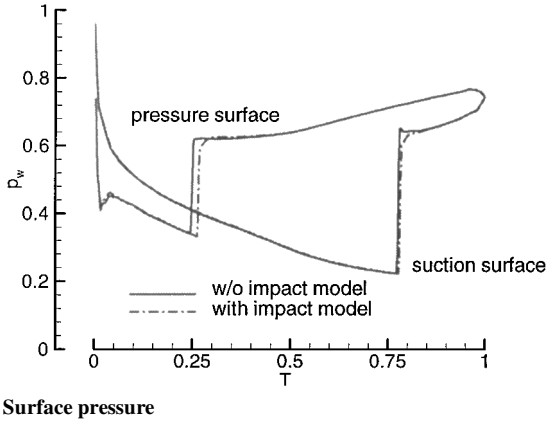

Surface pressure

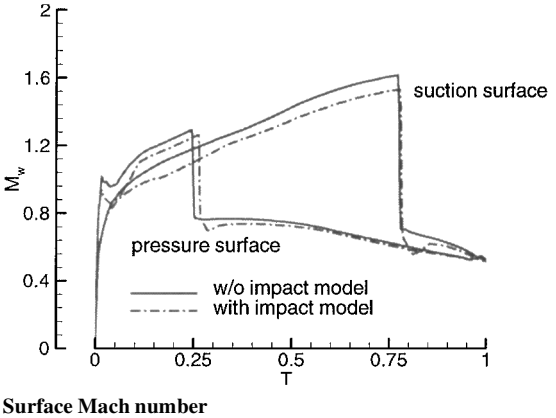

Surface Mach number

Fig. 18 Effect of droplet impact model on the blade properties.

can see from Figs. 17a and 17b. In this case, structural concern also arises. Change in the strength and position of the shock makes the cascade operate in the off-design condition. The possibility of blade resonance and material failure could emerge because the droplet effect studied so far can alter the structural load and overall vibration characteristics.

Finally, to see the effect of droplet impact on the blade, we calculated the passage flow dropping the droplet impact model. Overall, the flowfield appeared very similar to the earlier ones. As shown in Fig. 18, the surface pressure in the two cases remains about the same, whereas the overall surface velocity (or Mach number) is somewhat retarded when there is droplet impact. The average inlet Mach number also turned out about the same: 0.957 without the impact model and 0.955 with the impact model. This minor difference was also pointed out by Farrel and Vittal.[24]

Conclusions

The Lagrangian particle tracking method is implemented to the unstructured adaptive multigrid Euler solver to treat numerically the particle source terms iteratively interacting with the gas-phase flow. It is shown quantitatively that ingestion of the liquid droplets by the engine inlet can severely alter the aerodynamic characteristics of the cascade. Shock waves are weakened, as well as delayed, due to the relaxation effect of the droplets, whereas entropy is increased by the thermodynamic losses caused by the momentum transfer and heat transfer between the two phases. As a result, the inlet Mach number is decreased and the outlet Mach number is increased for a fixed outlet static pressure. Consequent pressure redistribution on the cascade blade surface is responsible for the overall performance degradation of the cascade.

References

[1] Valentine, J. R., and Decker, R. A., "Tracking of Raindrops in Flow over an Airfoil," *Journal of Aircraft*, Vol. 32, No. 1, 1995, pp. 100–105.

[2] Murthy, S. N. B., "Effect of Atmospheric Water Ingestion on the Performance and Operability of Flight Gas Turbines," AIAA Paper 96-3059, July 1996.

[3] Tabakoff, W., Hosny, W., and Hamed, A., "Effect of Solid Particles on Turbine Performance," *Journal of Engineering for Power*, Vol. 98, No. 1, Jan. 1976, pp. 47–52.

[4] Tsuchiya, T., and Murthy, S. N. B., "WISGSK-A Computer Code for the Prediction of a Multistage Axial Compressor Performance with Water Ingestion," NASA CR-3624, Sept. 1982.

[5] *Recommended Practices for the Assesment of the Effects of Atmospheric Water Ingestion on the Performance and Operability of Gas Turbine Engines*, AGARD Advisory Rept. 332, Sept. 1995.

[6] Anderson, W. K., and Bonhaus, D. L., "An Implicit Upwind Algorithm for Computing Turbulent Flows on Unstructured Grids," *Computers and Fluids*, Vol. 23, No. 1, 1994, pp. 1–21.

[7] Venkatakrishnan, V., "On the Accuracy of Limiters and Convergence to Steady State Solutions," AIAA Paper 93-0880, Jan. 1993.

[8] Lohner, R., "An Adaptive Finite Element Scheme for Transient Problems in CFD," *Computer Methods in Applied Mechanics and Engineering*, Vol. 61, No. 3, 1987, pp. 323–338.

[9] Bilanin, A. J., "Scaling Laws for Testing Airfoils Under Heavy Rainfall," *Journal of Aircraft*, Vol. 24, No. 1, 1987, pp. 31–37.

[10] Henderson, C. B., "Drag Coefficients of Spheres in Continuum and Rarefied Flows," *AIAA Journal*, Vol. 14, No. 6, 1976, pp. 707, 708.

[11] Carlson, D. J., and Hoglund, R. F., "Particle Drag and Heat Transfer in Rocket Nozzles," *AIAA Journal*, Vol. 2, No. 11, 1964, pp. 1980–1984.

[12] Crowe, C. T., Sharma, M. P., and Stock, D. E., "The Particle-Source-In Cell (PSI-CELL) Model for Gas-Droplet Flows," *Journal of Fluids Engineering*, Vol. 99, No. 2, 1977, pp. 325–332.

[13] Xu, H., Liu, Y., He, P., and Wang, H., "The TAR Model for Calculation of Droplet/Wall Impingement," *Journal of Fluids Engineering*, Vol. 120, No. 3, Sept. 1998, pp. 593–597.

[14] Park, K., and Watkins, A. P., "Comparison of Wall Spray Impaction Models with Experimental Data on Drop Velocities and Sizes," *International Journal of Heat and Fluid Flow*, Vol. 17, No. 4, 1996, pp. 424–438.

[15] Connel, S. D., and Holmes, D. G., "Three-Dimensional Unstructured Adaptive Multigrid Scheme for the Euler Equations," *AIAA Journal*, Vol. 32, No. 8, 1994, pp. 1626–1632.

[16]Parthasarathy, V., and Kallinderis, Y., "New Multigrid Approach for Three-Dimensional Unstructured, Adaptive Grids," *AIAA Journal*, Vol. 32, No. 5, 1994, pp. 956–963.

[17]Cuffel, R. F., Back, L. H., and Massier, P. F., "Transonic Flowfield in a Supersonic Nozzle with Small Throat Radius of Curvature," *AIAA Journal*, Vol. 7, No. 7, 1969, pp. 1364–1366.

[18]Serra, R. A., "Determination of Internal Gas Flows by a Transient Numerical Technique," *AIAA Journal*, Vol. 10, No. 5, 1972, pp. 603–611.

[19]Chang, I. S., "One- and Two-Phase Nozzle Flows," *AIAA Journal*, Vol. 18, No. 12, 1980, pp. 1455–1461.

[20]Ishii, R., and Umeda, Y., "Nozzle Flows and Gas-Particle Mixtures," *Physics of Fluids*, Vol. 30, No. 3, 1987, pp. 752–760.

[21]Hwang, C. J., and Chang, G. C., "Numerical Study of Gas-Particle Flow in a Solid Rocket Nozzle," *AIAA Journal*, Vol. 26, No. 6, 1988, pp. 682–689.

[22]Kang, I. M., and Chang, K. S., "Euler Analysis of Transonic Stator–Rotor Interaction Using a Finite Volume Method," *International Journal for Numerical Method in Fluids*, Vol. 12, No. 7, 1991, pp. 625–636.

[23]Giles, M. B., "Nonreflecting Boundary Condition for Euler Equation Calculations," *AIAA Journal*, Vol. 28, No. 12, 1990, pp. 2050–2058.

[24]Farrel, D. M., and Vittal, B. V. R., "Computer Simulation of Water Ingestion for the T800-LHT-801 Engine Anti-Icing Test Inlet," AIAA Paper 96-2652, July 1996.